Journal of Solid State Chemistry 184 (2011) 432–440

Contents lists available at ScienceDirect

Journal of Solid State Chemistry

journal homepage: www.elsevier.com/locate/jssc

Syntheses, and crystal and electronic structures of the new Zintl phases Na_2ACdSb_2 and K_2ACdSb_2 (A=Ca, Sr, Ba, Eu, Yb): Structural relationship with Yb_2CdSb_2 and the solid solutions $Sr_{2-x}A_xCdSb_2$, $Ba_{2-x}A_xCdSb_2$ and $Eu_{2-x}Yb_xCdSb_2$

Bayrammurad Saparov, Maia Saito, Svilen Bobev*

Department of Chemistry and Biochemistry, University of Delaware, Newark, DE 19716, USA

ARTICLE INFO

Article history:
Received 29 October 2010
Received in revised form
7 December 2010
Accepted 13 December 2010
Available online 21 December 2010

Keywords:
Zintl phases
Crystal structure
Single-crystal X-ray diffraction
Thermoelectric properties

ABSTRACT

Presented are the details of the syntheses, crystal and electronic structures of a new family of Zintl phases Na_2ACdSb_2 and K_2ACdSb_2 (A=Ca, Sr, Ba, Eu, Yb), as well as the solid solutions $Sr_{2-x}A_xCdSb_2$, $Ba_{2-x}A_xCdSb_2$ and $Eu_{2-x}Yb_xCdSb_2$. The structures of Na_2ACdSb_2 and K_2ACdSb_2 (A=Ca, Sr, Ba, Eu, Yb) were determined to be of a new type with the non-centrosymmetric space group $Pmc2_1$ (no. 26), Pearson symbol $oP12$, with lattice parameters a=4.684(1)−4.788(1) Å; b=9.099(3)−9.117(2) Å; c=7.837(1)−8.057(2) Å for the Na_2ACdSb_2 series, and a=4.6637(9)−5.0368(8) Å; b=9.100(2)−9.8183(15) Å; and c=7.7954(15)−8.4924(13) Å for K_2ACdSb_2, respectively. The solid solutions $Sr_{2-x}A_xCdSb_2$, $Ba_{2-x}A_xCdSb_2$ and $Eu_{2-x}Yb_xCdSb_2$ ($x\approx1$) are isostructural and isoelectronic to the recently reported Yb_2CdSb_2 (space group $Cmc2_1$ (no. 36), Pearson symbol $cP20$). All discussed structures are based upon $CdSb_2^{4-}$ polyanionic layers, similar to the ones observed in Yb_2CdSb_2, with various alkali- and/or alkaline-earth cations coordinated to them. Magnetic susceptibility and Seebeck coefficient measurements on selected $Eu_{2-x}Yb_xCdSb_2$ samples, taken at low temperatures up to 300 K, are also reported.

© 2010 Elsevier Inc. All rights reserved.

1. Introduction

Inspired by the captivating chemistry and physics of many pnictogen-based solid-state compounds [1–10], our group has been conducting a systematic study of new ternary, and more recently quaternary arsenides, antimonides and bismuthides. The past research efforts have been very successful and led to the discovery of numerous novel Zintl compounds such as $Ba_3Cd_2Sb_4$ [11], $Ba_2Cd_2As_3$ and $Ba_2Cd_2Sb_3$ [12], $A_{21}M_4Sb_{18}$ and $A_{21}Cd_4Bi_{18}$ [13,14], Ba_2ZnPn_2 [15], $A_{11}M_6Sb_{12}$ [16,17], $A_9M_{4+x}Sb_9$ and $A_9M_{4+x}Bi_9$ [18], $KA_2Cd_2Sb_3$ [19], among others (A=Ca, Sr, Ba, Eu, Yb; M=Zn, Cd; Pn=As, Sb, Bi). Deserving of specific mention here are the pair of compounds Yb_2CdSb_2 and Ca_2CdSb_2, also Zintl phases, which despite being isoelectronic adopt different structures: Yb_2CdSb_2 crystallizes in the non-centrosymmetric space group $Cmc2_1$, whereas Ca_2CdSb_2 crystallizes in the centrosymmetric space group $Pnma$ [20]. Such structural difference was considered rather surprising, given how close the ionic radii of similarly coordinated Yb^{2+} and Ca^{2+} cations are [21]. Nonetheless, both structures are very much alike (essentially polytypes), featuring $^2_\infty[CdSb_2]^{4-}$ polyanionic layers, made of corner-shared $CdSb_4$ tetrahedra, interspaced by Ca^{2+} or Yb^{2+} cations.

Building upon this work, we proceeded with experiments directed at both iso- and hetero-valent substitutions of Yb^{2+} and Ca^{2+} in Yb_2CdSb_2 and Ca_2CdSb_2, aimed at systematically studying the role of the cations as structure directing factors. Herein we report the results from this project, which include the synthesis of a new family of Zintl phases Na_2ACdSb_2 and K_2ACdSb_2 (A=Ca, Sr, Ba, Eu, Yb), as well as the solid solutions $Sr_{2-x}A_xCdSb_2$, $Ba_{2-x}A_xCdSb_2$ ($x\approx1$), and $Eu_{2-x}Yb_xCdSb_2$ ($1<x\leq2$). Via single-crystal and powder X-ray diffraction studies, it was established that Na_2ACdSb_2 and K_2ACdSb_2 crystallize with a novel structure type, largely similar to the Yb_2CdSb_2 structure [20]. The unique array of alkali- and alkaline-earth metal cations in both Na_2ACdSb_2 and K_2ACdSb_2, as well as the apparent cation site preferences in $Sr_{2-x}A_xCdSb_2$, $Ba_{2-x}A_xCdSb_2$ and $Eu_{2-x}Yb_xCdSb_2$, along with a summary of the electronic structures are also briefly reviewed. The temperature dependence of the Seebeck coefficients, measured on selected crystals from the solid solutions $Eu_{2-x}Yb_xCdSb_2$ (x=1.0, 1.6, 2.0) are discussed in conjunction with the data reported in the literature for other antimonide-based thermoelectric materials.

2. Experimental

2.1. Synthesis

All manipulations involving the reactive alkali- and alkaline-earth metals were carried out in an argon-filled glove box or under

* Corresponding author. Fax: +1 302 831 6335.
E-mail address: bobev@udel.edu (S. Bobev).

0022-4596/$ - see front matter © 2010 Elsevier Inc. All rights reserved.
doi:10.1016/j.jssc.2010.12.015

vacuum. Pure metallic elements, purchased from Alfa or Aldrich with purities greater than 99.9% (metal basis), were loaded in the desired stoichiometric ratios in niobium tubes, which were subsequently sealed using an arc-welder. The niobium tubes were then put in fused silica jackets, and flame-sealed under high vacuum. The reaction mixtures were subjected to different heat treatment in high temperature tube furnaces.

In order to synthesize the members of the Na_2ACdSb_2 and K_2ACdSb_2 series, where A = Ca, Sr, Ba, Eu, Yb, and to maximize yields of the successfully synthesized members, many different synthetic conditions were tried. The optimal conditions found involve quick heating of stoichiometric mixtures of the metals to 900 °C (at a rate of ca. 100 °C/h), a homogenization step at this temperature for 40 h, and then slowly cooling the melt to 600 °C (at a rate of 3 °C/h), followed by a dwell period at this temperature for 40 h. After this isothermal step, the tubes were cooled to 300 °C at a rate of 5 °C/h, at which point, the furnaces were switched off. The reactions were allowed to cool down to room temperature before the tubes were opened and the products were examined (done in the glove box). The typical products consisted of irregularly shaped black crystals, which were extremely air- and moisture-sensitive and thus, necessitated handling with extra care (see below). We note here that faster reactions with shorter cooling steps and dwell periods (heat to 900 °C at a rate of 100 °C/h, homogenized at 900 °C for 20 h, cooled to 600 °C at a rate of 5 °C/h, kept at 600 °C for 30 h, and eventually cooled to 300 °C at a rate of 5 °C/h) also afforded the title compounds in high yields, although the crystallinities were much poorer and the single-crystals were not suitable for X-ray diffraction work.

The synthesis of the solid solutions $Sr_{2-x}A_xCdSb_2$, $Ba_{2-x}A_xCdSb_2$ and $Eu_{2-x}Yb_xCdSb_2$ followed the optimized experimental procedure, described for Yb_2CdSb_2 [20]. For this purpose, the lead-flux method was employed. In a typical experiment, a mixture of two alkaline-earth metals (or Eu and Yb) in a ratio ca. 1:1 was combined with 1 equivalent Cd, 2 equivalents Sb and a large amount of Pb (e.g. 10-fold excess) in an alumina crucible, which was subsequently sealed under vacuum in a fused-silica tube. The reaction mixture was heated from room temperature to 960 °C at a rate of 200 °C/h, allowed to dwell at this temperature for 20 h, and then slowly cooled to 500 °C at a rate of 5 °C/h. The Pb-flux was subsequently removed and the products isolated. Such reactions yielded small needles of notably higher stability under ambient air, in comparison to Na_2ACdSb_2 and K_2ACdSb_2.

Although we tried many combinations of alkaline-earth metals in different ratios as part of this study, our efforts were not exhaustive, and hence, the complete solubility ranges in $Sr_{2-x}A_xCdSb_2$ and $Ba_{2-x}A_xCdSb_2$ are unknown. Based on our detailed syntheses for $Eu_{2-x}Yb_xCdSb_2$ ($0.9 < x \leq 2$) and on our previous work in the ternary systems Ca–Cd–Sb [20], Sr–Cd–Sb [18], Ba–Cd–Sb [11,12,14,17], Eu–Cd–Sb [16], and Yb–Cd–Sb [20], we can speculate that the homogeneity ranges are limited. Such a conclusion is also substantiated by the reactions with mixtures of two alkaline-earth metals (or Eu and Yb) in a ratio ca. 2:3, which yielded the known compounds $A_{11}Cd_6Sb_{12}$ [16,17] and $Ba_{3-x}A_xCd_2Sb_4$ [11]. Additional structural evidence suggests that the two cations tend to order on the two crystallographic sites (*vide infra*), making the nearly stoichiometric formulas $Sr_{1+x}A_{1-x}CdSb_2$ and $Ba_{1+x}A_{1-x}CdSb_2$ ($x \approx 0$) the optimal.

2.2. X-ray crystallography

X-ray powder diffraction data were collected on a Rigaku MiniFlex powder diffractometer, equipped with nickel-filtered Cu$K\alpha$ radiation. $\theta-\theta$ scans with a step size of 0.05° and a counting time of 3 s/step were used routinely. The instrument was operated inside a nitrogen-filled glove box to prevent contact of sample with air and moisture. Initial data analysis and phase identification was carried out using the JADE 6.5 package [22]. Le-Bail fits and refinements of the unit cell parameters for several samples where single-crystal quality was inadequate for further diffraction work (Table 1), were performed using GSAS [23]. Due to the complexity of the structure and the limited instrument resolution, refinements of the atomic coordinates were not carried out, but they were presumed isostructural with $Na_2YbCdSb_2$ (Table 1).

According to the powder patterns collected for specimens exposed to air even for very short periods of time (less than 1 h), the Na_2ACdSb_2 and K_2ACdSb_2 compounds are extremely air- and/or moisture-sensitive. The $Ba_{2-x}A_xCdSb_2$ phases appear moderately unstable under ambient air, while $Sr_{2-x}A_xCdSb_2$ and $Eu_{2-x}Yb_xCdSb_2$ were unchanged after several days on the bench-top.

Single-crystal X-ray diffraction data were acquired using a Bruker SMART CCD-based diffractometer equipped with monochromated Mo$K\alpha$ radiation (λ = 0.71073 Å). The crystals were picked under a microscope in the argon-filled glove box, cut to suitable dimensions, mounted on glass fibers with Paratone N oil, and transferred onto the goniometer. The data were collected at low temperatures using cold nitrogen stream, which also alleviated the problem with air-sensitivity of the samples. Several crystals from each batch were selected and checked for quality by rapid scans, before the best ones were chosen for further analysis. The data acquisition was carried out using the *SMART* software [24]; *SAINTplus* software package [25] was used for the integration and the global unit cell refinement from all data. Semi-empirical absorption correction was applied with *SADABS* [26]. The structures of Na_2ACdSb_2 and K_2ACdSb_2 (new type) were solved by direct methods and refined to convergence by full matrix least-squares methods on F^2, as implemented in *SHELXTL* [27]. In the final refinements, the coordinates were standardized using *STRUCTURE TIDY* [28]. The structures of $Sr_{2-x}A_xCdSb_2$, $Ba_{2-x}A_xCdSb_2$, and $Eu_{2-x}Yb_xCdSb_2$, which are isotypic with Yb_2CdSb_2 [20], were refined using the atomic positions from the published data. Refined parameters included the scale factor, the atomic positions with anisotropic displacement parameters, and occupancy factors for the mixed cation positions. Important data collection and structure refinement information for $K_2SrCdSb_2$, $K_2BaCdSb_2$, and $Na_2YbCdSb_2$ is provided in Table 1; positional and equivalent isotropic displacement parameters, and relevant

Table 1
Selected single-crystal data collection and structure refinement parameters for $K_2SrCdSb_2$, $K_2BaCdSb_2$ and $Na_2YbCdSb_2$.

Empirical formula	$K_2SrCdSb_2$	$K_2BaCdSb_2$	$Na_2YbCdSb_2$[a]
Formula weight	521.72	571.44	574.92
Crystal system		Orthorhombic	
Space group, Z		$Pmc2_1$ (no. 26), 2	
Temperature (K)		170(2)	
a (Å)	4.9317(12)	5.0366(8)	4.6637(9)
b (Å)	9.810(2)	9.8183(15)	9.100(2)
c (Å)	8.191(2)	8.4924(13)	7.7954(15)
Volume (Å^3)	396.3(2)	420.0(1)	330.9(1)
Density (calculated, g/cm^3)	4.372	4.519	5.771
Absorption coefficient (cm^{-1})	170.18	143.68	252.40
Reflections collected	5201	5614	4411
Independent reflections	1103	1163	924
Flack parameter	0.03(2)	0.21(4)	0.04(1)
R[b] indices [$I > 2\sigma_I$]	R_1 = 0.0303 wR_2 = 0.0691	R_1 = 0.0214 wR_2 = 0.0499	R_1 = 0.0220 wR_2 = 0.0462
Goodness-of-fit on F^2	1.051	1.072	1.008
Largest diff. peak/hole (e$^-$/Å^3)	1.50/−1.24	1.06/−0.68	1.33/−1.57

[a] Unit cell parameters for the isostructural $Na_2CaCdSb_2$ (a = 4.684(1) Å; b = 9.117(2) Å; c = 7.837(1) Å), $Na_2SrCdSb_2$ (a = 4.788(1) Å; b = 9.099(3) Å; c = 8.057(2) Å), and for $Na_2CaCdSb_2$ (a = 4.760(1) Å; b = 9.097(2) Å; c = 8.001(2) Å). Since single-crystal quality was poor, the cell constants were refined from the powder X-ray diffraction patterns with Si as an internal standard.

[b] $R_1 = \sum||F_o|-|F_c||/\sum|F_o|$; $wR_2 = [\sum[w(F_o^2-F_c^2)^2]/\sum[w(F_o^2)^2]]^{1/2}$, where $w = 1/[\sigma^2F_o^2+(AP)^2+BP]$, and $P = (F_o^2+2F_c^2)/3$; A and B are weight coefficients.

Table 2
Atomic coordinates and equivalent isotropic displacement parameters (U_{eq})[a] from single-crystal structure refinements for $K_2SrCdSb_2$, $K_2BaCdSb_2$ and $Na_2YbCdSb_2$.

Atom	Wyckoff site	x	y	z	U_{eq} (Å^2)
$K_2SrCdSb_2$					
K1	2*b*	1/2	0.4236(3)	0.0256(3)	0.0250(5)
K2	2*a*	0	0.3391(3)	0.3398(3)	0.0218(5)
Sr	2*a*	0	0.0459(1)	−0.0030(1)	0.0156(2)
Cd	2*b*	1/2	0.1758(1)	0.6521(1)	0.0177(2)
Sb1	2*b*	1/2	0.1100(1)	0.2831(1)	0.0147(2)
Sb2	2*a*	0	0.6850(1)	0.2479(1)	0.0168(2)
$K_2BaCdSb_2$					
K1	2*b*	1/2	0.4233(2)	0.0206(3)	0.0242(5)
K2	2*a*	0	0.3405(2)	0.3439(2)	0.0182(4)
Ba	2*a*	0	0.0496(1)	0.0000(1)	0.0126(1)
Cd	2*b*	1/2	0.1769(1)	0.6541(1)	0.0154(2)
Sb1	2*b*	1/2	0.1132(1)	0.2888(1)	0.0123(1)
Sb2	2*a*	0	0.6814(1)	0.2382(1)	0.0134(1)
$Na_2YbCdSb_2$					
Na1	2*b*	1/2	0.4203(6)	0.0506(6)	0.023(1)
Na2	2*a*	0	0.3315(5)	0.3683(6)	0.015(1)
Yb	2*a*	0	0.0556(1)	0.0000(1)	0.0153(1)
Cd	2*b*	1/2	0.1859(1)	0.6607(1)	0.0155(2)
Sb1	2*b*	1/2	0.1201(1)	0.2847(1)	0.0126(2)
Sb2	2*a*	0	0.6590(1)	0.2682(1)	0.0147(2)

[a] U_{eq} is defined as one-third of the trace of the orthogonalized U_{ij} tensor.

Table 3
Selected bond distances (Å) for $K_2SrCdSb_2$, $K_2BaCdSb_2$ and $Na_2YbCdSb_2$.

$K_2SrCdSb_2$		$K_2BaCdSb_2$		$Na_2YbCdSb_2$	
Atomic pair	Distance	Atomic pair	Distance	Atomic pair	Distance
K1–Sb2 (2 ×)	3.520(2)	K1–Sb2 (2 ×)	3.627(2)	Na1–Sb2 (2 ×)	3.287(4)
K1–Sb1 (1 ×)	3.731(3)	K1–Sb1 (1 ×)	3.803(2)	Na1–Sb1 (1 ×)	3.286(5)
K1–Sb2 (2 ×)	3.997(2)	K1–Sb2 (2 ×)	4.022(2)	Na1–Sb2 (2 ×)	3.610(4)
K2–Sb2 (1 ×)	3.351(3)	K2–Sb2 (1 ×)	3.355(2)	Na2–Sb2 (1 ×)	3.081(4)
K2–Sb1 (2 ×)	3.369(2)	K2–Sb1 (2 ×)	3.398(1)	Na2–Sb1 (2 ×)	3.092(3)
K2–Sb2 (1 ×)	3.476(3)	K2–Sb2 (1 ×)	3.465(2)	Na2–Sb2 (1 ×)	3.119(5)
Sr–Sb2 (1 ×)	3.337(1)	Ba–Sb2 (1 ×)	3.453(1)	Yb–Sb2 (1 ×)	3.164(1)
Sr–Sb1 (2 ×)	3.389(1)	Ba–Sb1 (2 ×)	3.480(1)	Yb–Sb1 (2 ×)	3.272(1)
Sr–Sb1 (2 ×)	3.459(1)	Ba–Sb1 (2 ×)	3.570(1)	Yb–Sb1 (2 ×)	3.288(1)
Sr–Cd (2 ×)	3.524(1)	Ba–Cd (2 ×)	3.606(1)	Yb–Cd (2 ×)	3.440(1)
Cd–Sb2 (2 ×)	2.926(1)	Cd–Sb2 (2 ×)	2.964(1)	Cd–Sb2 (2 ×)	2.852(1)
Cd–Sb1(1 ×)	3.002(1)	Cd–Sb1(1 ×)	3.070(1)	Cd–Sb1(1 ×)	2.947(1)
Cd–Sb1 (1 ×)	3.090(1)	Cd–Sb1 (1 ×)	3.165(1)	Cd–Sb1 (1 ×)	2.991(1)
Sb1–Cd (1 ×)	3.002(1)	Sb1–Cd (1 ×)	3.070(1)	Sb1–Cd (1 ×)	2.947(1)
Sb1–Cd (1 ×)	3.090(1)	Sb1–Cd (1 ×)	3.165(1)	Sb1–Cd (1 ×)	2.991(1)
Sb2–Cd (2 ×)	2.926(1)	Sb2–Cd (2 ×)	2.964(1)	Sb2–Cd (2 ×)	2.852(1)

interatomic distances for the three are listed in Tables 2 and 3, respectively. Data collection and structure refinement parameters for six $Sr_{2-x}A_xCdSb_2$ and $Ba_{2-x}A_xCdSb_2$ compounds are summarized in Table 4 [29]. Table 5 lists selected single-crystal data collection and refinement parameters for four members of the $Eu_{2-x}Yb_xCdSb_2$ solid solution series. Positional and equivalent isotropic displacement parameters, along with the occupancies of the mixed sites in $Sr_{2-x}A_xCdSb_2$, $Ba_{2-x}A_xCdSb_2$ and $Eu_{2-x}Yb_xCdSb_2$ can be found in Table 6. Further details of the crystal structure investigations can be obtained from Fachinformationszentrum Karlsruhe, 76344 Eggenstein-Leopoldshafen, Germany (fax: (49) 7247-808-666; e-mail: crysdata@fiz.karlsruhe.dea), on quoting the depository numbers: CSD-422273 for $K_2SrCdSb_2$, CSD-422272 for $K_2BaCdSb_2$, CSD-422724 for $Na_2YbCdSb_2$, CSD-422275 for $Sr_{1.06(1)}Ca_{0.94}CdSb_2$, CSD-422276 for $Sr_{1.16(1)}Yb_{0.84}CdSb_2$, CSD-422277 for $Ba_{0.97(1)}Ca_{1.03}CdSb_2$, CSD-422278 for $Ba_{0.89(2)}Sr_{1.11}CdSb_2$, CSD-422279 for $Ba_{0.92(1)}Eu_{1.08}CdSb_2$, CSD-422280 for $BaYbCdSb_2$, CSD-422281 for $Eu_{0.29(2)}Yb_{1.71}CdSb_2$, CSD-422282 for $Eu_{0.65(4)}Yb_{1.35}CdSb_2$, CSD-422283 for $Eu_{0.79(4)}Yb_{1.21}CdSb_2$, and CSD-422284 for $Eu_{1.07(3)}Yb_{0.93}CdSb_2$, respectively.

2.3. Electronic structure calculations

Tight-binding, linear muffin-tin orbital (TB-LMTO) calculations [30–33] were carried out for $K_2BaCdSb_2$, using the LMTO47 program [34]. This package employs the atomic sphere approximation (ASA) method, in which space is filled with overlapping Wigner–Seitz (WS) atomic spheres [35]. The WS radii were as follows: K=2.03–2.29 Å, Ba=1.84–2.23 Å, Cd=1.64 Å, Sb=1.80–1.89 Å. Exchange and correlation were treated by the local density approximation (LDA) [36]. All relativistic effects, except spin–orbit coupling, were taken into account by using a scalar relativistic approximation. The *k*-space integrations were conducted by the tetrahedron method [37], and the self-consistent charge density was obtained using 168 irreducible *k*-points in the Brillouin zone. The density of states (DOS) plots are presented herein with the Fermi level set as a reference point at 0 eV. In order to evaluate various orbital interactions, the crystal orbital Hamilton populations (COHP) [38] were also calculated.

2.4. Magnetic susceptibility measurements

Temperature-dependent magnetization (M) measurements were completed on a Quantum Design PPMS system. From practical considerations, only the $Eu_{2-x}Yb_xCdSb_2$ samples were measured. The specimens were prepared in the glove-box by loading 10–20 mg of single-crystals, picked under a microscope into specially designed holders [39]. The measurements were done in the temperature interval 5–300 K in an applied field (H) of 1000 Oe (field cooling mode). The gathered magnetization data were converted to magnetic susceptibility ($\chi_m = M/H$), normalized per-mol rare-earth metal.

2.5. Seebeck coefficient measurements

Measurements of Seebeck coefficients as a function of the temperature were carried out using the commercially available system from MMR Technologies. The instrument uses expansion of grade 5 Argon (99.999%) to attain low temperatures employing the Joule–Thompson effect. Small needle-shaped crystals were picked under a microscope and attached to sample holder using silver paste (SPI). For each sample, a constantan wire of comparable dimensions (diameter=0.01″) was cut and used as a reference material. After mounting the crystal and the reference material, and allowing the silver paste cure, the samples were put inside the Seebeck coefficient measurement chamber. The chamber was evacuated for at least 30 min (below 10 mTorr) before beginning the data acquisition (done twice—on cooling and heating). Temperature range was 100–300 K and the cooling/heating rate was 10 K/min. Each measurement was repeated at least twice and more than two crystals from each reaction batch were measured to ensure reproducibility. Due to the air-sensitivity of Na_2ACdSb_2, K_2ACdSb_2, and the Ba-containing $Ba_{2-x}A_xCdSb_2$ compounds, measurements for these samples were not possible. Consistent data ($\pm$16%) could only be obtained for the solid solutions $Eu_{2-x}Yb_xCdSb_2$ (x=1.0, 1.6, 2.0).

2.6. Electrical resistivity measurements

Measurements of the electrical resistivity as a function of the temperature were carried out using a commercial PPMS system (Quantum Design) in the range 10–300 K. Because suitable single-crystals were not available, four-probe measurements could not be performed for all samples. The reported herein data were obtained by the two-probe method, and therefore only

Table 4
Selected single-crystal data collection and structure refinement parameters for $Sr_{2-x}A_xCdSb_2$ and $Ba_{2-x}A_xCdSb_2$.

Empirical formula	$Sr_{1.06(1)}Ca_{0.94}CdSb_2$	$Sr_{1.16(1)}Yb_{0.84}CdSb_2$	$Ba_{0.97(1)}Ca_{1.03}CdSb_2$	$Ba_{0.89(2)}Sr_{1.11}CdSb_2$	$Ba_{0.92(1)}Eu_{1.08}CdSb_2$	$BaYbCdSb_2$
Formula weight	486.69	603.11	530.65	575.52	646.37	666.28
Crystal system			Orthorhombic			
Space group, Z			$Cmc2_1$ (no. 36), 4			
Temperature (K)			120(2)			
a (Å)	4.6808(17)	4.6855(11)	4.7223(6)	4.810(3)	4.8016(4)	4.7186(12)
b (Å)	18.043(7)	18.035(4)	18.622(2)	18.427(10)	18.5054(17)	18.608(5)
c (Å)	7.328(3)	7.3284(17)	7.3899(9)	7.743(5)	7.6100(7)	7.3686(18)
Volume (Å^3)	618.9(4)	619.3(2)	649.9(1)	686.2(7)	676.2(1)	647.0(3)
Density (calculated, g/cm^3)	5.223	6.469	5.424	5.571	6.349	6.840
Absorption coefficient (cm^{-1})	217.70	343.37	179.30	242.79	259.87	316.36
Reflections collected	3387	3432	3858	1540	3967	3364
Independent reflections	765	763	741	759	768	735
Flack parameter	0.17(1)	0.18(1)	0.11(5)	0.03(2)	0.02(2)	0.04(1)
R^a indices [$I > 2\sigma_I$]	$R1 = 0.0184$ $wR2 = 0.0393$	$R1 = 0.0148$ $wR2 = 0.0330$	$R1 = 0.0200$ $wR2 = 0.0419$	$R1 = 0.0269$ $wR2 = 0.0635$	$R1 = 0.0123$ $wR2 = 0.0253$	$R1 = 0.0148$ $wR2 = 0.0313$
Goodness-of-fit on F^2	1.070	1.068	1.034	1.043	1.058	0.982
Largest diff. peak/hole (e$^-$/Å^3)	1.21/−1.29	0.98/−1.17	0.85/−0.79	0.99/−1.41	0.73/−0.54	0.82/−1.31

[a] $R_1 = \sum||F_o| - |F_c||/\sum|F_o|$; $wR_2 = [\sum[w(F_o^2 - F_c^2)^2]/\sum[w(F_o^2)^2]]^{1/2}$, where $w = 1/[\sigma^2F_o^2 + (AP)^2 + BP]$, and $P = (F_o^2 + 2F_c^2)/3$; A and B are weight coefficients.

Table 5
Selected single-crystal data collection and structure refinement parameters for $Eu_{2-x}Yb_xCdSb_2$.

Empirical formula	$Eu_{0.29(2)}Yb_{1.71}CdSb_2$	$Eu_{0.65(4)}Yb_{1.35}CdSb_2$	$Eu_{0.79(4)}Yb_{1.21}CdSb_2$	$Eu_{1.07(3)}Yb_{0.93}CdSb_2$
Formula weight	695.76	688.38	685.22	679.53
Crystal system		Orthorhombic		
Space group, Z		$Cmc2_1$ (no. 36), 4		
Temperature (K)		120(2)		
a (Å)	4.6360(13)	4.6423(12)	4.6554(16)	4.682(2)
b (Å)	17.554(5)	17.630(4)	17.727(6)	17.841(8)
c (Å)	7.202(2)	7.2134(18)	7.231(3)	7.291(3)
Volume (Å^3)	586.1(3)	590.4(3)	596.8(4)	609.0(5)
Density (calculated, g/cm^3)	7.885	7.745	7.627	7.411
Absorption coefficient (cm^{-1})	425.54	404.17	392.11	370.55
Reflections collected	3097	3104	2235	3300
Independent reflections	683	682	690	748
R^a indices [$I > 2\sigma_I$]	$R_1 = 0.0164$ $wR_2 = 0.0372$	$R_1 = 0.0211$ $wR_2 = 0.0493$	$R_1 = 0.0199$ $wR_2 = 0.0487$	$R_1 = 0.0176$ $wR_2 = 0.0380$
Goodness-of-fit on F^2	1.086	1.148	1.172	1.066
Largest diff. peak/hole (e$^-$/Å^3)	1.45/−1.83	1.54/−3.19	1.63/−2.79	0.87/−1.43

[a] $R_1 = \sum||F_o| - |F_c||/\sum|F_o|$; $wR_2 = [\sum[w(F_o^2 - F_c^2)^2]/\sum[w(F_o^2)^2]]^{1/2}$, where $w = 1/[\sigma^2F_o^2 + (AP)^2 + BP]$, and $P = (F_o^2 + 2F_c^2)/3$; A and B are weight coefficients.

qualitatively illustrate the temperature dependence. A more accurate four-probe electrical resistivity value for Yb_2CdSb_2 was taken from Ref. [20], and was used in the estimates of the thermoelectric power factor.

3. Results and discussion

3.1. Crystal structure of Na_2ACdSb_2 and K_2ACdSb_2

Na_2ACdSb_2 and K_2ACdSb_2 (A = Ca, Sr, Ba, Eu, Yb) are novel isoelectronic and isostructural phases, which crystallize in their own type with the primitive orthorhombic space group $Pmc2_1$ (Pearson symbol $oP12$) [40]. There are six unique crystallographic positions in the asymmetric unit of the structure (Fig. 1), including two alkali metal sites, one alkaline-earth or rare-earth metal site, one cadmium and two antimony sites. All atoms are in special positions with mirror symmetries. In the following paragraphs, we have chosen to focus the attention on one of them, $K_2BaCdSb_2$, as a representative of the group. It is the second structurally characterized phase in the corresponding K–Ba–Cd–Sb quaternary system, after $KBa_2Cd_2Sb_3$ ($Ca_3Al_2Ge_3$ type) [19].

The crystal structure of $K_2BaCdSb_2$ can be rationalized following the Zintl–Klemm concept [41–44] as $^2_\infty[CdSb_2]^{4-}$ polyanionic layers, made of corner-shared $CdSb_4$ tetrahedra, and K^+ and Ba^{2+} cations (Fig. 1). The formal electron count for this Zintl phase can be then expressed as $(K^+)_2(Ba^{2+})(Cd^{2+})(Sb^{3-})_2$ or $(K^+)_2(Ba^{2+})(4b\text{-}Cd^{2-})(2b\text{-}Sb^{1-})_2$. The layers are stacked along the crystallographic b-axis in a similar fashion to the layers in Yb_2CdSb_2 [20], and the $Sr_{2-x}A_xCdSb_2$, $Ba_{2-x}A_xCdSb_2$, and $Eu_{2-x}Yb_xCdSb_2$ solid solutions discussed later on (Fig. 2). From the figures, it is evident that the latter structure is reminiscent to the atomic arrangement in $K_2BaCdSb_2$, and could be considered as the product of a hetero-valent substitution of the two alkali metal cations in $K_2BaCdSb_2$ with a single alkaline-earth metal. Aside from the different nature/number of cations, the most notable difference between the two structures is the stacking order—in order for the $K_2BaCdSb_2$ structure to accommodate the extra cation (as compared to a hypothetical Ba_2CdSb_2 with the Yb_2CdSb_2 type with only one cation between the $^2_\infty[CdSb_2]^{4-}$ layers), every second layer must be shifted by $\vec{a}/2$. This, essentially, is the reason as to why the $K_2BaCdSb_2$ structure cannot form with the C-centered space group of Yb_2CdSb_2.

Drawing on this structural parallel, we must also mention the difference in the cation polyhedra in both structures. In $K_2BaCdSb_2$,

Table 6
Atomic coordinates, equivalent isotropic displacement parameters (U_{eq})[a] and occupation factors from single-crystal structure refinements for $Sr_{2-x}A_xCdSb_2$, $Ba_{2-x}A_xCdSb_2$, $Eu_{0.29(2)}Yb_{1.71}CdSb_2$ and $Eu_{1.07(3)}Yb_{0.93}CdSb_2$.

Atom	Wyckoff site	x	y	z	U_{eq} (Å^2)	Occupation
$Sr_{1.06(1)}Ca_{0.94}CdSb_2$						
*A*1	4*a*	0	0.3019(1)	0.5254(1)	0.0124(3)	$Sr_{0.96(1)}Ca_{0.04}$
*A*2	4*a*	0	0.4785(1)	0.2234(2)	0.0118(5)	$Sr_{0.10(1)}Ca_{0.90}$
Cd	4*a*	0	0.0969(1)	0.3934(1)	0.0118(1)	1
Sb1	4*a*	0	0.0631(1)	0.0042(1)	0.0101(1)	1
Sb2	4*a*	0	0.3274(1)	0.0067(1)	0.0116(1)	1
$Sr_{1.16(1)}Yb_{0.84}CdSb_2$						
*A*1	4*a*	0	0.3016(1)	0.5253(1)	0.0132(3)	$Sr_{0.98(1)}Yb_{0.02}$
*A*2	4*a*	0	0.4791(1)	0.2232(1)	0.0107(1)	$Sr_{0.18(1)}Yb_{0.82}$
Cd	4*a*	0	0.0962(1)	0.3942(1)	0.0121(1)	1
Sb1	4*a*	0	0.0636(1)	0.0042(1)	0.0107(1)	1
Sb2	4*a*	0	0.3279(1)	0.0061(1)	0.0120(1)	1
$Ba_{0.97(1)}Ca_{1.03}CdSb_2$						
*A*1	4*a*	0	0.3022(1)	0.5240(1)	0.0098(2)	$Ba_{0.97(1)}Ca_{0.03}$
*A*2	4*a*	0	0.4790(1)	0.2241(3)	0.0097(4)	$Ba_{0.0}Ca_{1.0}$
Cd	4*a*	0	0.0947(1)	0.3936(1)	0.0107(2)	1
Sb1	4*a*	0	0.0590(1)	0.0059(1)	0.0085(2)	1
Sb2	4*a*	0	0.3330(1)	0.0069(1)	0.0099(2)	1
$Ba_{0.89(2)}Sr_{1.11}CdSb_2$						
*A*1	4*a*	0	0.2982(4)	0.5366(1)	0.0130(3)	$Ba_{0.84(2)}Sr_{0.16}$
*A*2	4*a*	0	0.4763(1)	0.2258(2)	0.0113(4)	$Ba_{0.05(1)}Sr_{0.95}$
Cd	4*a*	0	0.0932(1)	0.3876(2)	0.0116(2)	1
Sb1	4*a*	0	0.0627(1)	0.0108(1)	0.0096(12)	1
Sb2	4*a*	0	0.3321(1)	−0.0153(1)	0.0125(2)	1
$Ba_{0.92(1)}Eu_{1.08}CdSb_2$						
*A*1	4*a*	0	0.2993(1)	0.5292(1)	0.0111(2)	$Ba_{0.92(1)}Eu_{0.08}$
*A*2	4*a*	0	0.4783(1)	0.2261(1)	0.0096(1)	$Ba_{0.0}Eu_{1.0}$
Cd	4*a*	0	0.0930(1)	0.3917(1)	0.0105(1)	1
Sb1	4*a*	0	0.0619(1)	0.0097(1)	0.0088(1)	1
Sb2	4*a*	0	0.3329(1)	−0.0081(1)	0.0106(1)	1
$BaYbCdSb_2$						
*A*1	4*a*	0	0.3021(1)	0.5237(1)	0.0094(1)	$Ba_{1.0}Yb_{0.0}$
*A*2	4*a*	0	0.4797(1)	0.2243(1)	0.0093(1)	$Ba_{0.0}Yb_{1.0}$
Cd	4*a*	0	0.0941(1)	0.3945(1)	0.0101(2)	1
Sb1	4*a*	0	0.0592(1)	0.0055(1)	0.0083(2)	1
Sb2	4*a*	0	0.3336(1)	0.0079(1)	0.0094(2)	1
$Eu_{0.29(2)}Yb_{1.71}CdSb_2$						
*A*1	4*a*	0	0.3024(1)	0.5287(1)	0.0111(2)	$Eu_{0.29(2)}Yb_{0.71}$
*A*2	4*a*	0	0.4789(1)	0.2199(1)	0.0085(2)	$Eu_{0.0}Yb_{1.0}$
Cd	4*a*	0	0.0984(1)	0.3941(1)	0.0091(2)	1
Sb1	4*a*	0	0.0663(1)	−0.0008(1)	0.0075(2)	1
Sb2	4*a*	0	0.3231(1)	0.0090(1)	0.0095(2)	1
$Eu_{1.07(3)}Yb_{0.93}CdSb_2$						
*A*1	4*a*	0	0.3018(1)	0.5298(7)	0.0142(2)	$Eu_{0.89(2)}Yb_{0.11}$
*A*2	4*a*	0	0.4789(1)	0.2224(8)	0.0119(2)	$Eu_{0.18(3)}Yb_{0.82}$
Cd	4*a*	0	0.0973(1)	0.3945(1)	0.0126(2)	1
Sb1	4*a*	0	0.0647(1)	0.0025(1)	0.0111(2)	1
Sb2	4*a*	0	0.3259(1)	0.0065(1)	0.0128(2)	1

[a] U_{eq} is defined as one-third of the trace of the orthogonalized U_{ij} tensor.

the K cations fill the space between the polyanionic layers (Fig. 1), taking on the same role as the Yb1 atom in Yb_2CdSb_2 (dubbed the interlayer position) [20]. While the Yb1 in the later structure is octahedrally coordinated, the two K positions in $K_2BaCdSb_2$ have different coordination polyhedra—the environment around K1 consists of five Sb atoms in square pyramidal arrangement, and K2 is surrounded by four Sb atoms in distorted tetrahedral geometry (Fig. 3). The Ba atoms are surrounded by five Sb atoms occupying the corners of a square pyramid—the same exact coordination environment as the Yb2 site in Yb_2CdSb_2 [20]. Ba–Sb and K–Sb distances also match those reported for $KBa_2Cd_2Sb_3$ [19], with the exception of K1–Sb distances, which are on average much longer than K2–Sb distances (Table 3).

There are no homoatomic Sb–Sb bonds in the $K_2BaCdSb_2$ structure. The Cd–Sb distances (Table 3) are comparable to those

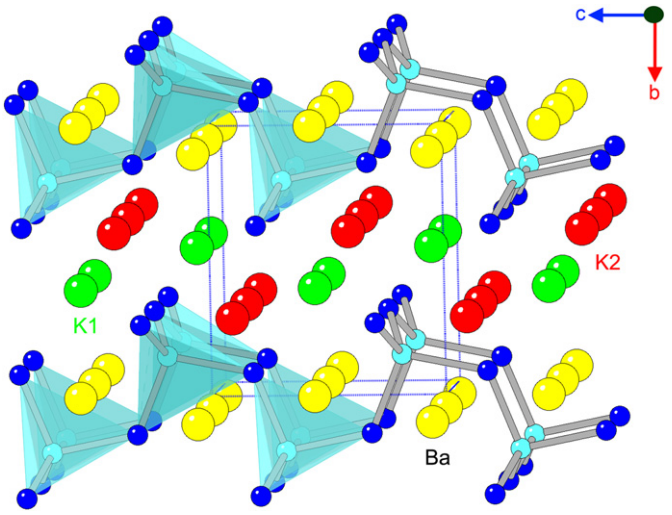

Fig. 1. Combined ball-and-stick and polyhedral representations of the orthorhombic $K_2BaCdSb_2$ structure (own type), viewed down *a*-axis. Unit cell is outlined. The polyanionic $^{2}_{\infty}[CdSb_2]^{4-}$ layers, made of corner-shared $CdSb_4$ tetrahedra, are emphasized. Online color: Cd atoms are colored in light blue; Sb atoms are shown as deep blue spheres. The Ba, K1 and K2 atoms are drawn as yellow, green and red spheres, respectively. (For interpretation of the references to color in this figure legend, the reader is referred to the web version of this article.)

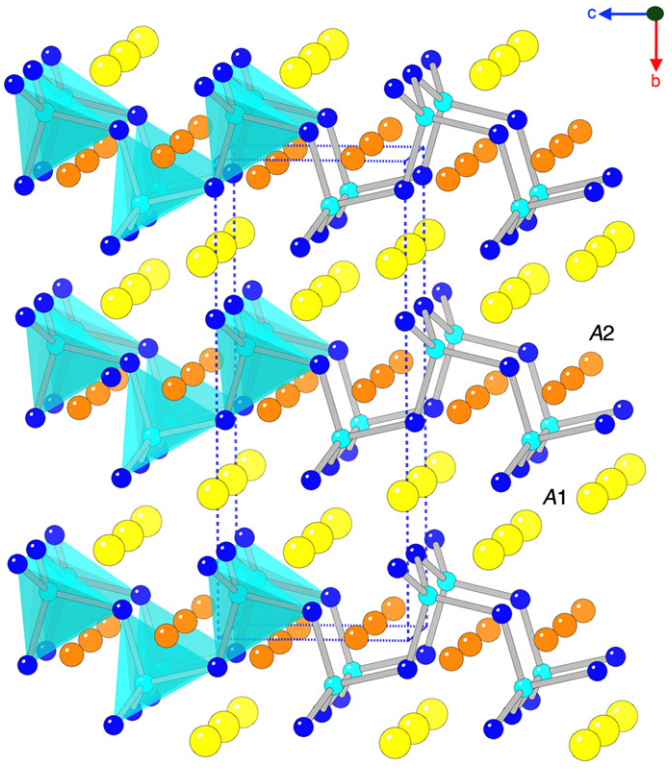

Fig. 2. Combined ball-and-stick and polyhedral representations of the orthorhombic structure of $Sr_{2-x}A_xCdSb_2$, $Ba_{2-x}A_xCdSb_2$, and $Eu_{2-x}Yb_xCdSb_2$ (Yb_2CdSb_2 type), viewed down the *b*-axis. Unit cell is outlined. Online color: Cd atoms are colored in light blue; Sb atoms are shown as deep blue spheres. The inter- and intra-layer cations are drawn as yellow and orange spheres, respectively. (For interpretation of the references to color in this figure legend, the reader is referred to the web version of this article.)

reported for other Zintl phases with structures based on $CdSb_4$ tetrahedra, such as $Ba_3Cd_2Sb_4$ [11], $Ba_2Cd_2Sb_3$ [12], $Ba_{21}Cd_4Sb_{18}$ [14], $Eu_{11}Cd_6Sb_{12}$ [16], Yb_2CdSb_2 and Ca_2CdSb_2 [20], NaCdSb [45], etc. The Cd–Sb distances are slightly shorter in $K_2SrCdSb_2$ than in

$K_2BaCdSb_2$; they are significantly shorter in $Na_2YbCdSb_2$ (Table 3). This can be traced back to the unit cell dimensions across the series as a function of the cation size—notice how the *a*- and *c*-axis vary on going from $K_2SrCdSb_2$ to $K_2BaCdSb_2$, and from $Na_2YbCdSb_2$ to $Na_2SrCdSb_2$, while the *b*-axis remains almost the same if the alkali metal does not change. This, of course is not unexpected, considering the fact that the size of the intralayer alkaline-earth metal will determine the magnitude of the *a*- and *c*-axis, which affects the Cd–Sb bonding as well. The dimension *b* is largely dependent on the size of the interlayer alkali metals.

3.2. Crystal structure of $Sr_{2-x}A_xCdSb_2$, $Ba_{2-x}A_xCdSb_2$, and $Eu_{2-x}Yb_xCdSb_2$

As mentioned already, these adopt the Yb_2CdSb_2 type (space group $Cmc2_1$; Pearson symbol *oC*20) with similar $^2_\infty[CdSb_2]^{4-}$ layers (Fig. 2). For in-depth structural analysis and further discussion, we refer to the original article on Yb_2CdSb_2 [20]. Here, we will briefly discuss some intricacies with regard to the solid solutions.

During the original work on Yb_2CdSb_2 and Ca_2CdSb_2 [20], we noted that isostructural compounds with Sr, Ba and Eu could not be synthesized. Subsequently, we carried out structural studies for another related structure, that of $Ba_3Cd_2Sb_4$ [11], and discovered a tendency for atomic order among chemically similar, but spatially different alkaline-earth/rare-earth metals in $Ba_{3-x}A_xCd_2Sb_4$ (*A*=Ca, Sr, Eu, Yb). This peculiarity made us look back at the *A*–Ca–Cd–Sb and *A*–Yb–Cd–Sb systems, with the aim to exploit the marked difference between inter- and intra-layer cations in terms of coordination number and distances to neighboring Sb atoms to synthesize quaternary variants of Yb_2CdSb_2 and Ca_2CdSb_2. This work resulted in the synthesis of the solid solutions $Sr_{2-x}A_xCdSb_2$, $Ba_{2-x}A_xCdSb_2$, and $Eu_{2-x}Yb_xCdSb_2$.

In the initial trials, the experiments were set up with a stoichiometric ratio 1:1:1:2, anticipating the formation of line compounds. Our idea was that by combining the smaller Ca (r=1.970 Å), Yb (r=1.933 Å) with the bigger Sr (r=2.148 Å), Ba (r=2.215 Å), and Eu (r=2.084 Å) [21], one could expect "coloring" of the cation sites. Such tendency to order can be understood from simple geometrical reasoning—the interlayer site with octahedral coordination of Sb's (*A*1, Table 6) will be exclusively occupied by the larger cation, and the intralayer site with square pyramidal arrangement of Sb atoms surrounding it (*A*2, Table 6) will be occupied by the smaller cation. The data from the refined structures of $Ba_{0.97(1)}Ca_{1.03}CdSb_2$ and $BaYbCdSb_2$ confirm there is no mixing of elements on the cation sites [46]. In $Ba_{0.92(1)}Eu_{1.08}CdSb_2$, the 6-coordinated *A*1 refines as nearly fully occupied Ba, while the 5-coordinated *A*2 show preferential occupation by Eu. For all other $Sr_{2-x}A_xCdSb_2$ and $Eu_{2-x}Yb_xCdSb_2$ structures, both cation positions are shared by the two cations (Table 6), albeit mixing is rather limited in range with preferential occupation by a single cation (ca. 70–98%).

While we did not set out to investigate the full solubility ranges, based on the 10 refined structures reported here, and based on extensive previous experience, we can speculate that a full range of solid solution is not likely to exist in any system. For $Ba_{2-x}A_xCdSb_2$ (Table 4), which are the phases with the strictest site preferences and the smallest phase widths, this can easily be related to the fact that the size difference between the cations in these cases is the greatest. For $Sr_{2-x}A_xCdSb_2$ and $Eu_{2-x}Yb_xCdSb_2$, mixing is more pronounced as the size difference between the cations is smaller. We investigated $Eu_{2-x}Yb_xCdSb_2$ (x=1, 1.2, 1.4, 1.6) in more detail and found that the four reactions loaded with x=0.2 increments yield samples with refined compositions very close to the nominal ones (Table 5). Also, for $Eu_{0.29(2)}Yb_{1.71}CdSb_2$, Eu atoms are all in the interlayer site (*A*1). Increasing the Eu amount does eventually result in small substitution of Yb atoms in the intralayer position as well, but the trend described above holds (Table 6). However, attempts to further increase the amount of Eu that substitutes for Yb failed and led to phase separation.

3.3. Bonding and electronic structures

The electronic structure of $K_2BaCdSb_2$, a representative of the novel structure type is discussed in detail next. The electronic structures of $Sr_{2-x}A_xCdSb_2$, $Ba_{2-x}A_xCdSb_2$, and $Eu_{2-x}Yb_xCdSb_2$ are expected to be similar to Ca_2CdSb_2 and Yb_2CdSb_2, which are discussed elsewhere [20].

The band diagram, the density-of-states (DOS) and the crystal orbital Hamilton population (COHP) plots for $K_2BaCdSb_2$ are provided in Fig. 4. The results of the electronic structure calculations indicate nearly optimized bonding interactions and are in full agreement with the Zintl formalism [41–44], mentioned earlier. According to it, $K_2BaCdSb_2$ is a salt-like material and the charge-balance can be denoted as $(K^+)_2(Ba^{2+})(Cd^{2+})(Sb^{3-})_2$.

As seen from the plot of the total density of states (TDOS), there is a small band gap at the Fermi level, which is a typical characteristic of many Zintl phases [43,44]. The partial DOS plots for Ba and K show minimal contribution to the total DOS around the Fermi level, suggesting largely space-filler and electron donor roles of the cations in these compounds, as in the classical Zintl description. It is interesting to note here that Ba cations in related ternary antimonides, such as $Ba_3Cd_2Sb_4$ [11], $Ba_2Cd_2Sb_3$ [12] and Ba_2ZnSb_2 [15], among others, have more significant contributions to the DOS around the Fermi level, thereby implying a higher degree of covalency of the Ba–Sb interactions.

To further analyze the roles of cations in $K_2BaCdSb_2$, we refer to the COHP plots. They show that the bonding in the polyanionic $^2_\infty[CdSb_2]^{4-}$ layers is optimized, as expected. The Ba–Sb bonding states are filled at the Fermi level, with some slightly bonding or non-bonding states left unfilled above the Fermi level. The integrated COHP values (–iCOHP) for the cation–anion interactions reveal that, although their contributions to the total DOS are low, Ba and Sr atoms are distinctly different than the K atoms. Thus, if Ba–Sb and K–Sb interactions are compared by the respective –iCOHPs, it becomes obvious that the K–Sb bonding is ca. 3.5–4 times weaker than Ba–Sb. This finding can be related to the distribution of the cations over the three crystallographic positions,

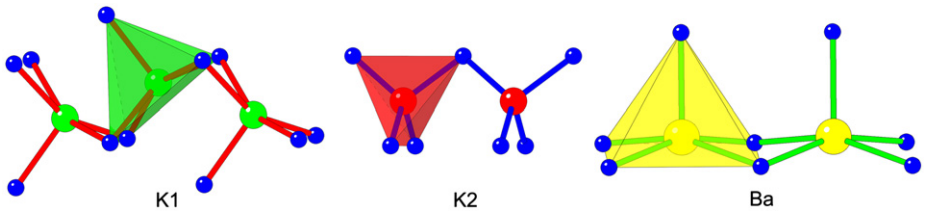

Fig. 3. Coordination polyhedra of the three cations in the $K_2BaCdSb_2$ structure. Online color: Cd atoms are colored in light blue; Sb atoms are shown as deep blue spheres. The Ba, K1 and K2 atoms are drawn as yellow, green and red spheres, respectively. (For interpretation of the references to color in this figure legend, the reader is referred to the web version of this article.)

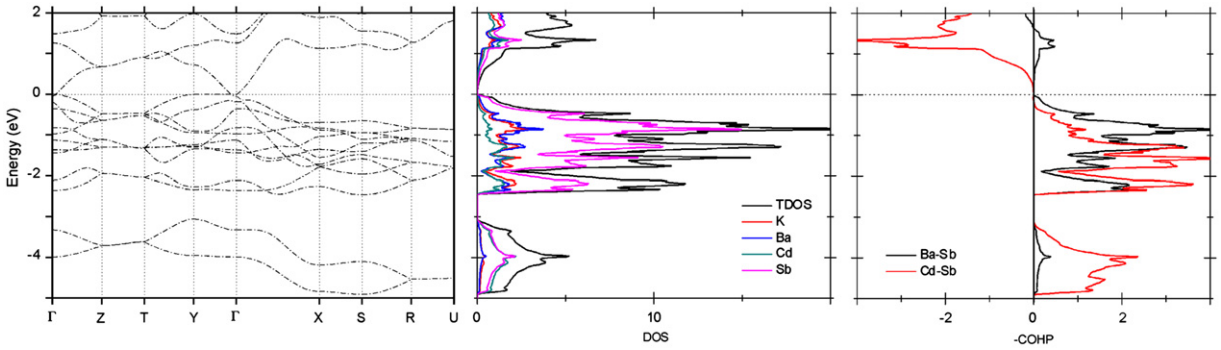

Fig. 4. Band diagram, DOS and COHP curves for $K_2BaCdSb_2$. Total DOS curves are shown with a solid line; partial DOS are shown as shaded areas. E_F (solid line) is the energy reference at 0 eV. In the COHP curves, the values are inverted so that the "+" regions represent bonding interactions, and the "−" regions represent antibonding interactions, respectively. Color online: partial DOS of K, Ba, Cd and Sb are represented by red, blue, green and dark cyan, respectively. (For interpretation of the references to color in this figure legend, the reader is referred to the web version of this article.)

which apparently ensures a maximum number of close Ba–Sb, and conversely, a minimum number of K–Sb short distances. Recall that the K2 atoms occupy a tetrahedral hole in $K_2BaCdSb_2$ (Fig. 3), compared to the Ba atoms, which occupy the square pyramidal site (CN=5). The K1 site is also five-coordinated (Fig. 3), however, the K1 atoms are farther away from the closest Sb neighbors compared to the alkaline-earth metal (see Table 3 for comparison of the respective K–Sb and Ba–Sb distances in $K_2BaCdSb_2$). Such results corroborate our earlier observations regarding the different roles of the alkali and alkaline-earth metal atoms in $KBa_2Cd_2Sb_3$ and $KSr_2Cd_2Sb_3$ [19].

3.4. Physical properties

The magnetic susceptibility of three $Eu_{2-x}Yb_xCdSb_2$ samples with varied Eu content was determined in applied fields of 500 Oe or 1000 Oe. The measured specimens were carefully selected under microscope single-crystals in random orientations. The temperature dependence of the molar magnetic susceptibility (χ_m) and the inverse susceptibility for the most Eu-rich $Eu_{1.07(3)}Yb_{0.93}CdSb_2$ material are plotted in Fig. 5; the data for the other two samples can be found in the Supplementary material section. As seen from the figures $1/\chi_m$ versus temperature is indicative of the fact that the samples are paramagnetic and that the magnetic behavior follows the Curie–Weiss law [47]. The calculated moments (μ_{eff}) and the Weiss temperatures (θ_p) obtained from these fits are 8.06 μ_B and −1.29 K for $Eu_{1.07(3)}Yb_{0.93}CdSb_2$, 7.98 μ_B and 0.51 K for $Eu_{0.65(4)}Yb_{1.35}CdSb_2$, 7.98 μ_B and 1.76 K for $Eu_{0.29(2)}Yb_{1.71}CdSb_2$, respectively. No magnetic phase transitions were observed in the measured temperature interval (down to 5 K), although ordering could be achieved by cooling the samples to even lower temperatures, as inferred from the Weiss temperatures.

The effective moment values are in a good agreement with the magnetic moment of 7.94 μ_B expected for the free-ion Eu^{2+} with seven unpaired electrons [47]. These numbers also confirm divalent ytterbium in $Eu_{2-x}Yb_xCdSb_2$ ($\mu_{eff}=0$ μ_B for free-ion Yb^{2+}, $[Xe]4f^{14}$ configuration) [46], matching very well the data for Yb_2CdSb_2 [20] and corroborating the Zintl electron count.

High Seebeck coefficient is a prerequisite for a high thermoelectric figure of merit, $zT=\alpha^2T/\kappa\rho$, where α is the Seebeck coefficient, T the absolute temperature, κ the thermal conductivity, and ρ the electrical resistivity. Zintl compounds have long been thought to provide a balance between high Seebeck coefficients and the low electrical resistivity values [10,48,49]. Very recently, it has been shown that this balance can be even further fine-tuned via solid solutions, as in $Ca_xYb_{1-x}Zn_2Sb_2$ for example [7].

With this idea in mind, we carried out the syntheses and the measurements of the Seebeck coefficient on Eu-substituted

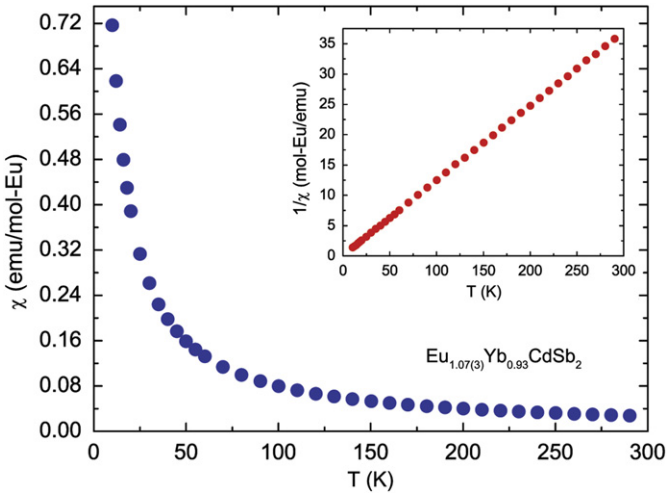

Fig. 5. Plot of the magnetic susceptibility ($\chi=M/H$) versus T for $Eu_{1.07(3)}Yb_{0.93}CdSb_2$. Data are collected in a field-cooling mode ($H=1000$ Oe) and normalized per mol-Eu. Inset: Inverse susceptibility (χ^{-1}) as a function of the temperature.

Yb_2CdSb_2 samples $Eu_{2-x}Yb_xCdSb_2$ ($x=1.0$, 1.6, 2.0). The data are presented in Fig. 6, according to which the dominant charge carriers are holes, and the samples are p-type semiconductors. The highest Seebeck coefficient (217 μV/K at RT) was observed for Yb_2CdSb_2, while the lowest Seebeck coefficient (133 μV/K at RT), and therefore more metallic properties, was observed for the most heavily doped material. This is somewhat difficult to explain as the electronegativity of Eu is lower than that of Yb [50], and based on this alone, one could expect the inverse dependence upon substitution of Eu for Yb. The temperature dependence of the Seebeck coefficient shows a nearly linear increase with increasing temperature, which is typical of metals and heavily doped degenerate semiconductors. The high values of the Seebeck coefficient are characteristic of the semiconductors [7,10]. The numerical values of the Seebeck coefficients at room temperature are very high, and are comparable to some of the best known high zT Zintl phases such as AZn_2Sb_2 (A=Ca, Sr, Eu, Yb) family (48–159 μV/K) [9], the solid solutions $Ca_xYb_{1-x}Zn_2Sb_2$ (48–120 μV/K) [7], $CaCd_2Sb_2$ (265 μV/K) [51], $YbCd_2Sb_2$ (ca. 115 μV/K) [52], $EuCd_2Sb_2$ (233 μV/K) [51], and higher than $Yb_{14}MnSb_{11}$ (60 μV/K) [3].

The power factor α^2/ρ could be calculated as well using the reported temperature dependent electrical resistivity data for Yb_2CdSb_2. The resistivity of 2.25 mΩ cm and the Seebeck coefficient of 217 μV/K at room temperature result in a high power

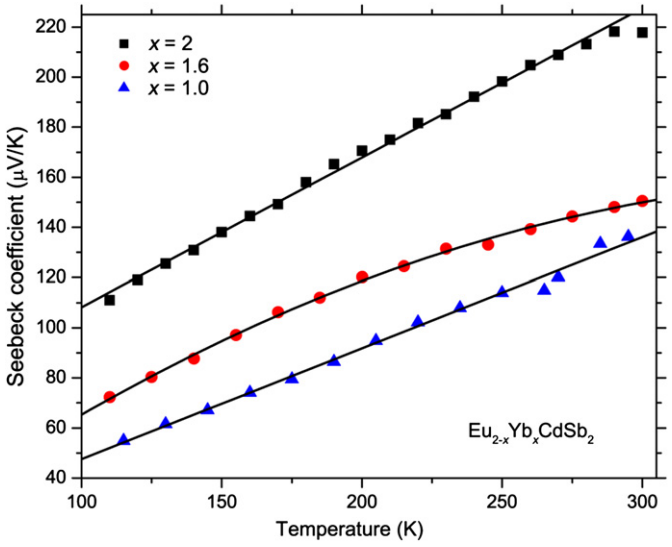

Fig. 6. Seebeck coefficient vs. T for $Eu_{2-x}Yb_xCdSb_2$ ($x=1.0$; 1.6; 2.0).

factor of 20.93 μW/(cm K^2) comparable to that of $EuZn_2Sb_2$ (ca. 17 μW/(cm K^2)) [53], but higher than the reported values for $EuCd_2Sb_2$ (ca. 6 μW/(cm K^2)) [53], $CaCd_2Sb_2$ (below 1 μW/(cm K^2)) [51], $YbCd_2Sb_2$ (ca. 6 μW/(cm K^2)) [52], $CaZn_2Sb_2$ (6.076 μW/(cm K^2)) [9], $YbZn_2Sb_2$ (7.2 μW/(cm K^2)) [52], etc. All of the above suggests a promise for high zT (provided the thermal conductivities are low) and calls for more work on these materials.

4. Conclusions

We have successfully synthesized and characterized a new family of quaternary Zintl compounds Na_2ACdSb_2 and K_2ACdSb_2 (A=Ca, Sr, Ba, Eu, Yb), as well as the solid solutions $Sr_{2-x}A_xCdSb_2$, $Ba_{2-x}A_xCdSb_2$ ($x\approx1$), and $Eu_{2-x}Yb_xCdSb_2$ ($1<x\leq2$). Their crystal structures can be rationalized as made of polyanionic $^2_\infty[CdSb_2]^{4-}$ layers, with cations separating them. The layers are similar to those reported for the isoelectronic Yb_2CdSb_2 and Ca_2CdSb_2 [20]. The computed electronic structure of $K_2BaCdSb_2$ confirms that the title compounds are narrow-gap semiconductors in agreement with the Zintl formalism. The small gaps indicate good prospects for thermoelectric applications, especially in the light of the large number of well-known high efficiency thermoelectric materials based on antimonides. However, the extreme sensitivity to air/moisture of Na_2ACdSb_2 and K_2ACdSb_2, hampers the physical property measurements and appears to be a limitation of this family for practical applications. Transport properties of the $Eu_{2-x}Yb_xCdSb_2$ ($1<x\leq2$) samples, which are among the most stable ones, were measured—the determined values yield very high power factor of 20.93 μW/(cm K^2), suggesting that they might be promising candidates for more optimization runs.

Acknowledgments

Svilen Bobev acknowledges financial support from the University of Delaware and the Petroleum Research Fund (ACS-PRF). Maia Saito thanks the NSF Summer Research Program in Solid State Chemistry for the 2010 REU fellowship. The authors are indebted to Prof. K.V. Ramanujachary (Rowan University, Glassboro, NJ, USA) for the repeat magnetic susceptibility measurement on the $Eu_{2-x}Yb_xCdSb_2$ samples.

Appendix A. Supplementary materials

Supplementary data associated with this article can be found in the online version at doi:10.1016/j.jssc.2010.12.015.

References

[1] Y. Kamihara, T. Watanabe, M. Hirano, H. Hosono, J. Am. Chem. Soc. 130 (2008) 3296.
[2] J.H. Tapp, Z. Tang, B. Lv, K. Sasmal, B. Lorenz, P.C.W. Chu, A.M. Guloy, Phys. Rev. B 78 (2008) 060505 R.
[3] S.R. Brown, S.M. Kauzlarich, F. Gascoin, G.J. Snyder, Chem. Mater. 18 (2006) 1873.
[4] M. Rotter, M. Tegel, D. Johrendt, Phys. Rev. Lett. 101 (2008) 107006.
[5] K. Sasmal, B. Lv, B. Lorenz, A. Guloy, F. Chen, Y.-Y. Xue, C.-W. Chu, Phys. Rev. Lett. 101 (2008) 107007.
[6] J.-T. Han, J.-S. Zhou, J.-G. Cheng, J.B. Goodenough, J. Am. Chem. Soc. 132 (2010) 908.
[7] F. Gascoin, S. Ottensmann, D. Stark, S.M. Haïle, G.J. Snyder, Adv. Funct. Mater. 15 (2005) 1860.
[8] H. Zhang, J.T. Zhao, Yu. Grin, X.J. Wang, M.B. Tang, Z.Y. Man, H.H. Chen, X.X. Yang, J. Chem. Phys. 129 (2008) 164713.
[9] E.S. Toberer, A.F. May, B.C. Melot, E. Flage-Larsen, G.J. Snyder, Dalton Trans. 39 (2010) 1046.
[10] G.J. Snyder, E.S. Toberer, Nat. Mater. 7 (2008) 105.
[11] B. Saparov, S.-Q. Xia, S. Bobev, Inorg. Chem. 47 (2008) 11237.
[12] B. Saparov, H. He, X.H. Zhang, R. Greene, S. Bobev, Dalton Trans. 39 (2010) 1063.
[13] S.-Q. Xia, S. Bobev, Inorg. Chem. 46 (2007) 874.
[14] S.-Q. Xia, S. Bobev, Inorg. Chem. 47 (2008) 1919.
[15] B. Saparov, S. Bobev, Inorg. Chem. 49 (2010) 5173.
[16] B. Saparov, S. Bobev, A. Ozbay, E.R. Nowak, J. Solid State Chem. 181 (2008) 2690.
[17] S.-Q. Xia, S. Bobev, J. Comput. Chem. 29 (2008) 2125.
[18] S.-Q. Xia, S. Bobev, J. Am. Chem. Soc. 129 (2007) 10011.
[19] B. Saparov, M. Broda, K.V. Ramanujachary, S. Bobev, Polyhedron 29 (2010) 456.
[20] S.-Q. Xia, S. Bobev, J. Am. Chem. Soc. 129 (2007) 4049.
[21] L. Pauling, The Nature of the Chemical Bond, Cornell University Press, Ithaca, NY, 1960.
[22] JADE Version 6.5, Materials Data Inc., Livermore, CA, 2003.
[23] A. C. Larson, R. B. Von Dreele, GSAS—General Structure Analysis System; LAUR 86-748, Los Alamos National Laboratory, Los Alamos, NM, 1994.
[24] SMART NT, version 5.63, Bruker Analytical X-ray Systems Inc., Madison, WI, USA, 2003.
[25] SAINT NT, version 6.45, Bruker Analytical X-ray Systems Inc., Madison, WI, USA, 2003.
[26] G.M. Sheldrick, SADABS, University of Göttingen, Germany, 2003.
[27] G.M. Sheldrick, SHELXTL, University of Göttingen, Germany, 2001.
[28] L.M. Gelato, E. Parthe, J. Appl. Crystallogr. 20 (1987) 139.
[29] Elemental micro-analysis by means of energy-dispersive X-ray spectrometry (JEOL 7400F electron microscope equipped with an INCA-OXFORD detector) confirmed only the elemental make-up of the title compounds. The analyses could not provide more accurate compositions than the ones established from the refinement of the single-crystal X-ray data (due to the air-sensitivity of the samples, lack of proper calibration standards, etc.). Since the mixed-occupied sites usually contain elements with very different Z-numbers, the refined chemical formulas are deemed reliable. A plot of the unit cell volume variation of $Eu_{2-x}Yb_xCdSb_2$ ($1<x\leq2$) as a function of the Eu:Yb ratio is given in the supplementary information section—therein, despite the poorer Z-contrast between Eu and Yb, the refined compositions nicely follow the Vegard's law.
[30] O.K. Andersen, Phys. Rev. B 12 (1975) 3060.
[31] O.K. Andersen, O. Jepsen, Phys. Rev. Lett. 53 (1984) 2571.
[32] O.K. Andersen, O. Jepsen, D. Glötzel, in: F. Bassani, F. Fumi, M.P. Tosi (Eds.), Highlights of Condensed Matter Theory, North-Holland, New York, , 1985.
[33] O.K. Andersen, Phys. Rev. B 34 (1986) 2439.
[34] O. Jepsen, O.K. Andersen, TB-LMTO-ASA Program, Version 4.7, Max-Planck Institut für Festkörperforschung, Stuttgart, Germany, 1998.
[35] O. Jepsen, O.K. Andersen, Z. Phys. B 97 (1995) 35.
[36] U. von Barth, L. Hedin, J. Phys. C: Solid State Phys. 5 (1972) 1629.
[37] P.E. Blöchl, O. Jepsen, O.K. Andersen, Phys. Rev. B: Condens. Matter 49 (1994) 16223.
[38] R. Dronskowski, P.E. Blöchl, J. Phys. Chem. 97 (1993) 8617.
[39] S.-Q. Xia, S. Bobev, Inorg. Chem. 45 (2006) 7126.
[40] P. Villars, L.D. Calvert (Eds.), 2nd ed., American Society for Metals, Materials Park, OH, USA, , 1991 (and the desktop edition 1997).
[41] E. Zintl, Angew. Chem. 52 (1939) 1.
[42] H. Schäfer, Annu. Rev. Mater. Sci. 5 (1985) 1.
[43] R. Nesper, Prog. Solid State Chem. 20 (1990) 1.
[44] S.M. Kauzlarich (Ed.), VCH, New York, , 1996 and the references therein.
[45] G. Nuspl, K. Polborn, J. Evers, G.A. Landrum, R. Hoffmann, Inorg. Chem. 35 (1996) 6922.
[46] In the case of $BaYbCdSb_2$, the structure was refined as fully ordered with no mixing at all, and for $Ba_{0.97(1)}Ca_{1.03}CdSb_2$ the mixing, if any, is at the limits of the statistical significance.
[47] C. Kittel, Solid State Physics, Academic Press, New York, 1968.

[48] S.M. Kauzlarich, S.R. Brown, G.J. Snyder, Dalton Trans. 21 (2007) 2099.
[49] E.S. Toberer, A.F. May, G.J. Snyder, Chem. Mater. 22 (2010) 624.
[50] Note that there are certain difficulties when comparing the electronegativities of *d*- and *f*-block elements due to a number of factors, such as variable oxidation states and ambiguities in determining the valence electron density. For such reasons, the commonly used Pauling's scale [21] cannot be relied upon here. We refer to J.K. Nagle, J. Am. Chem. Soc. 112 (1990) 4741.
[51] H. Zhang, L. Fang, M.-B. Tang, H.-H. Chen, X.-X. Yang, X. Guo, J.-T. Zhao, Y. Grin, Intermetallics 18 (2010) 193.
[52] Q.-G. Cao, H. Zhang, M.-B. Tang, H.-H. Chen, X.-X. Yang, Y. Grin, J.-T. Zhao, J. Appl. Phys. 107 (2010) 053714.
[53] H. Zhang, M. Baitinger, M.-B. Tang, Z.-Y. Man, H.-H. Chen, X.-X. Yang, Y. Liu, L. Chen, Y. Grin, J.-T. Zhao, Dalton Trans. 39 (2010) 1101.